Science Advances
AAAS

advances.sciencemag.org/cgi/content/full/5/1/eaau8149/DC1

Supplementary Materials for

Metastable asymmetrical structure of a shaftless V_1 motor

Shintaro Maruyama, Kano Suzuki, Motonori Imamura, Hikaru Sasaki, Hideyuki Matsunami, Kenji Mizutani, Yasuko Saito, Fabiana L. Imai, Yoshiko Ishizuka-Katsura, Tomomi Kimura-Someya, Mikako Shirouzu, Takayuki Uchihashi, Toshio Ando, Ichiro Yamato, Takeshi Murata*

*Corresponding author. Email: t.murata@faculty.chiba-u.jp

Published 30 January 2019, *Sci. Adv.* **5**, eaau8149 (2019)
DOI: 10.1126/sciadv.aau8149

The PDF file includes:

Other Supplementary Material for this manuscript includes the following:

(available at advances.sciencemag.org/cgi/content/full/5/1/eaau8149/DC1)

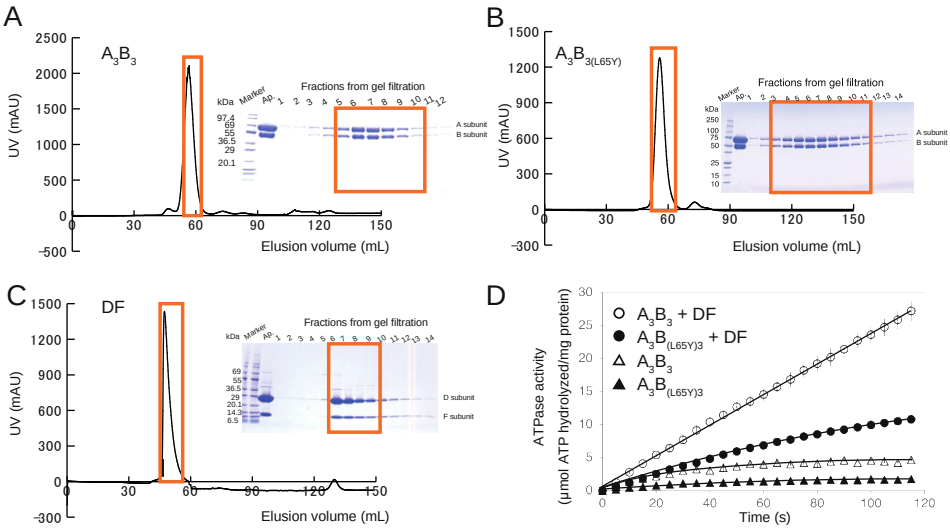

Fig. S1. Purification and ATPase activity of wild-type A_3B_3, mutant $A_3B_{(L65Y)3}$, and DF complexes. (**A-C**) Gel filtration profiles of A_3B_3 (A), $A_3B_{(L65Y)3}$ (B), and DF (C) complexes applied on HiLoad 16/60 Superdex 200 pg (A, B) or HiLoad 16/60 Superdex 75 pg (C) columns. SDS-PAGE patterns of samples obtained during the purification procedure are shown on the right side. Fractions surrounded by square boxes in the gel filtration profiles correspond to those in SDS-PAGE and were pooled as purified samples. (**D**) ATPase activities of the purified samples were measured using an ATP regeneration system. ATP hydrolysis rates at 23°C were determined by measuring the rate of NADH oxidation, which was defined by a decrease in absorbance at 340 nm. Wild-type A_3B_3 had low activity, but the activity increased by reconstitution of V_1 with DF complex. Mutant $A_3B_{(L65Y)3}$ had very low activity, which also increased in the presence of DF. Standard deviations are shown with straight bars.

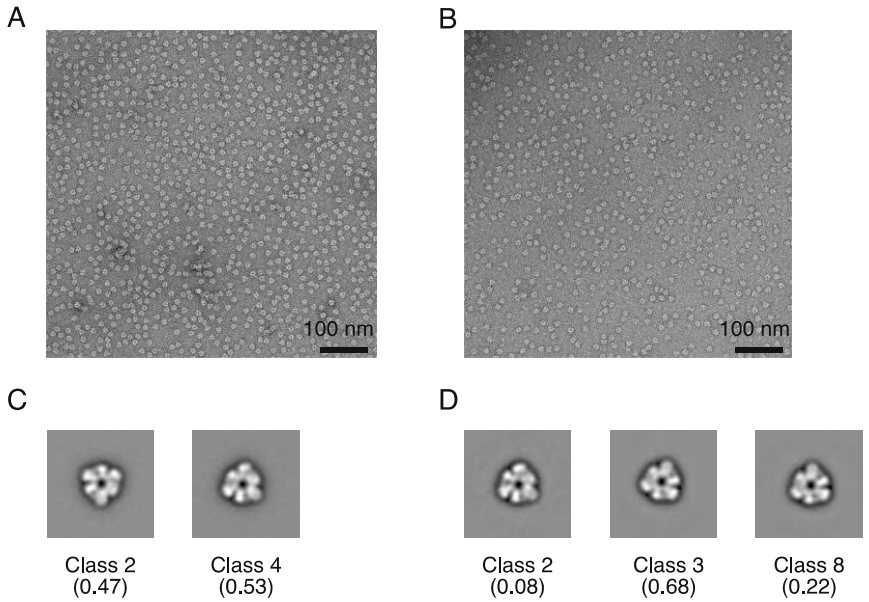

Fig. S2. Electron micrographs of negatively stained wild-type and mutant A_3B_3 complexes. Representative images of the wild-type (**A**) and mutant (**B**) A_3B_3 complexes are shown. The scale bar corresponds to 100 nm. After manual particle selection for reference, 5097 particles were selected from 12 images of the wild-type molecules, while 15933 particles from 60 images of the mutant molecules. The calculated reference-free two-dimensional class averaged images from the wild-type (**C**) and mutant (**D**) A_3B_3 complexes converged into two and three classes, respectively. Two-dimensional class averaging of the images revealed two classes with 0.47, 0.53 for wild-type A_3B_3 and three classes with 0.08, 0.68, and 0.22 for the mutant A_3B_3. The fractions of each class are shown in parentheses.

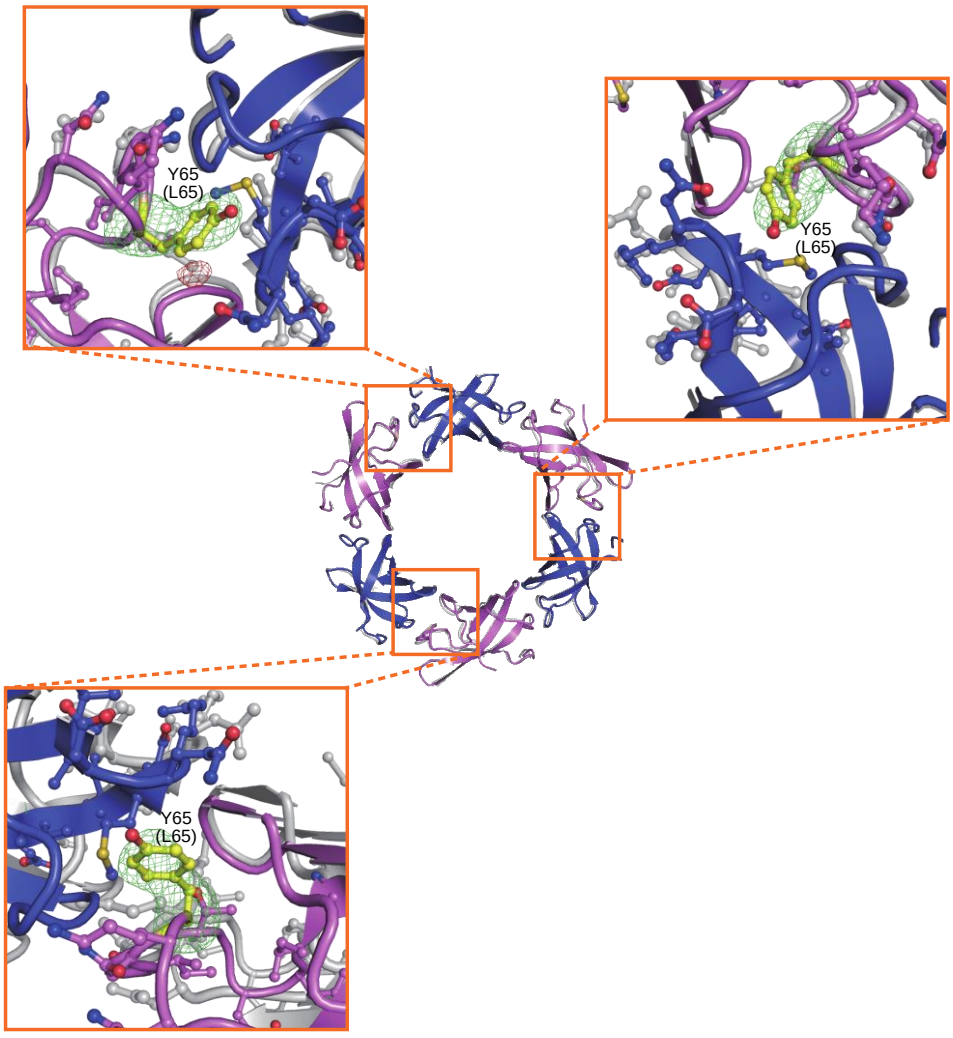

Fig. S3. Comparison of the crown structures of wild-type and mutant A_3B_3 complexes. The β-barrel domain (crown) of mutant $A_3B_{(L65Y)3}$ was superimposed at the 'bindable' form onto that of wild-type. A_3B_3 mutant is shown as a blue or purple drawing as in Fig. 1 and wild-type is shown in grey. Orange squares in the central figure indicate the mutated sites. (Surrounding figures) Magnified pictures of the mutated sites show the mutated amino acid residue (L65Y) in yellow. The $|F_o|$-$|F_c|$ omit map of L65Y residue at 4.0 sigma is shown by red (negative) and green (positive) meshes.

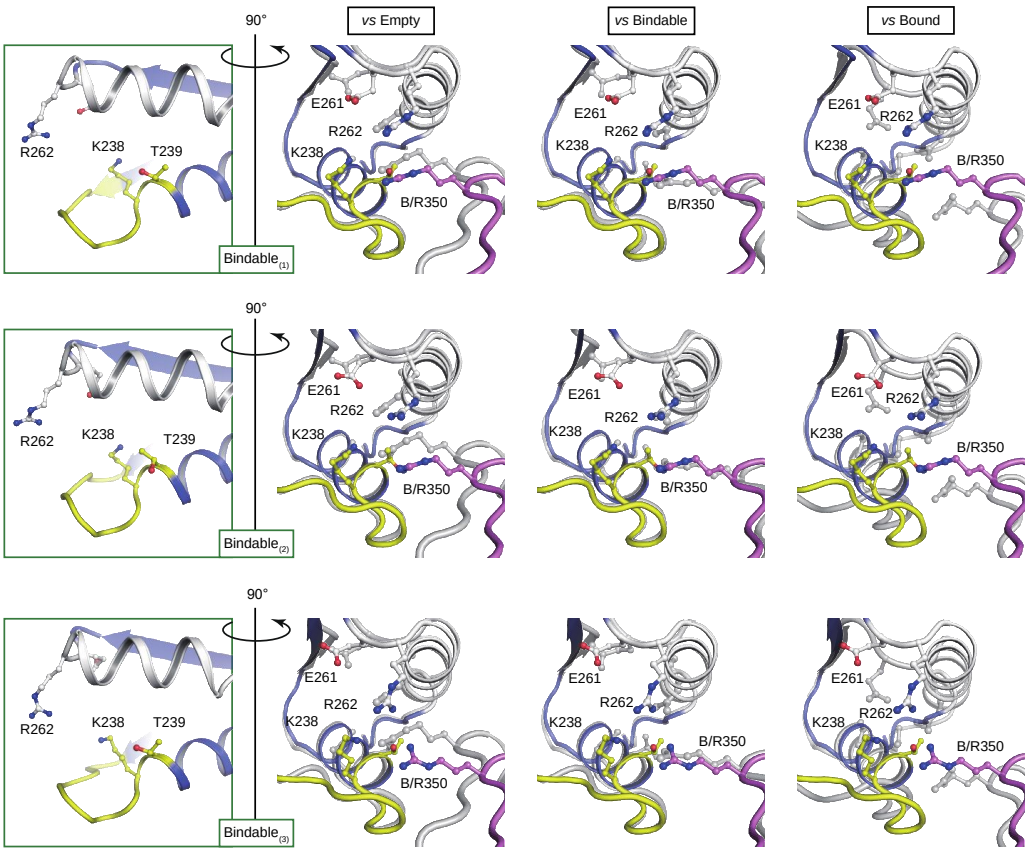

Fig. S4. Magnified views of the nucleotide binding sites of the bindable forms in $eA_3B_{(L65Y)3}$. The nucleotide binding sites, corresponding to the green box in Fig. 3E, are shown with conserved residues. The P-loop and 'arm' are depicted by the yellow and white ribbon representations, respectively, similar to those in Fig. 4E-G. The three panels on the right display an A-B interface that was rotated 90° around a vertical axis from the figures on the far-left. 'Bindable$_{(1)\text{-}(3)}$' forms in $eA_3B_{(L65Y)3}$ (color) are superimposed at the A subunit (residues 67-593) with 'empty', 'bindable', and 'bound' in eA_3B_3 (grey) with relevant amino acid residues.

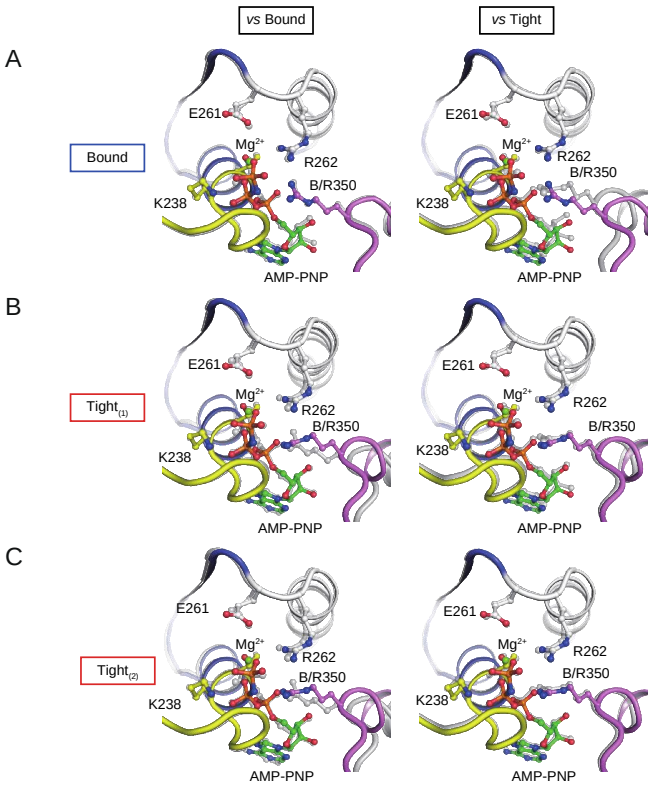

Fig. S5. Comparison of the nucleotide binding sites of wild-type and mutant complexes. 'Bound' (**A**), 'tight$_{(1)}$' (**B**), and 'tight$_{(2)}$' (**C**) forms in b$A_3B_{(L65Y)3}$ are shown similar to the right columns in Fig. 4E-G, and are superimposed at the A subunit (residues 67-593) with the 'bound' form in the b$A_3B_{(L65Y)3}$ (grey, left column) and 'tight' form in bV_1 (grey, right column).

Table S1. Data collection and refinement statistics.

	$eA_3B_{(L65Y)3}$	$bA_3B_{(L65Y)3}$
Data collection		
Space group	$P2_1$	$P2_12_12_1$
Cell dimensions		
Unit cell a, b, c (Å)	180.84, 107.77, 193.37	105.83, 151.37, 235.49
Unit cell α, β, γ (°)	90, 99.39, 90	90, 90, 90
Resolution (Å)	50-3.38 (3.59-3.38)	60-2.10 (2.23-2.10)
R_{merge}	0.113 (0.674)	0.124 (0.837)
Mean I / σ(I)	15.77 (2.90)	11.32 (2.11)
Completeness (%)	99.0 (94.2)	99.5 (97.5)
Redundancy	6.7 (6.4)	6.6 (6.2)
Refinement		
Resolution (Å)	48.20-3.38	54.87-2.10
No. reflections	101796	218240
R_{work} / R_{free}	0.2151/0.2575	0.1659/0.1955
No. atoms		
Protein	47887	24467
Ligand/ion	0	342
Water	100	1299
B-factors		
Protein	108.80	38.63
Ligand/ion	-	54.25
Water	53.43	40.55
R.m.s. deviations		
Bond lengths (Å)	0.002	0.006
Bond angles (°)	0.435	0.774
Ramachandran favoured (%)	98.0	98.7
Ramachandran allowed (%)	1.9	1.3
Ramachandran outliers (%)	0.0	0.0
PDB ID	5ZEA	5ZE9

Numbers in parentheses are for the highest resolution shell.

I / σ(I), intensity divided by error of intensity; R, residual factor

Table S2. RMSD values in superimpositions for each A_1B_1 unit of $eA_3B_{(L65Y)3}$ in the crystal structures of A_3B_3 and V_1 complexes.

Structure	Form	$eA_3B_{(L65Y)3}$		
	A_1B_1 unit	$Bindable_{(1)}$	$Bindable_{(2)}$	$Bindable_{(3)}$
eA_3B_3	Empty	1.30	1.65	2.29
	Bindable	1.02	0.88	1.21
	Bound	3.58	3.26	2.87
bA_3B_3	Empty	1.33	1.60	2.16
	$Bound_{(1)}$	3.84	3.59	3.35
	$Bound_{(2)}$	4.01	3.76	3.52
bV_1	Empty	1.56	1.83	2.39
	Bound	4.12	3.85	3.54
	Tight	4.79	4.61	4.48
$eA_3B_{(L65Y)3}$	$Bindable_{(1)}$	0	0.75	1.46
	$Bindable_{(2)}$	0.75	0	1.14
	$Bindable_{(3)}$	1.46	1.14	0

The values were calculated using Cα atoms.

Table S3. Contact surface areas between A and B subunits in various A_1B_1 forms (Å^2).

Structure	A_1B_1 form[a]	Contact surface (Å^2)
eA_3B_3	Empty	2243.2
	Bindable	1812.7
	Bound	2293.7
bA_3B_3	Empty	2379.9
	$Bound_{(1)}$	2448.2
	$Bound_{(2)}$	2560.6
bV_1	Empty	2291.0
	Bound	2488.0
	Tight	3130.7
$eA_3B_{(L65Y)3}$	$Bindable_{(1)}$	1998.6
	$Bindable_{(2)}$	1959.1
	$Bindable_{(3)}$	1982.4
$bA_3B_{(L65Y)3}$	$Tight_{(1)}$	3026.5
	Bound	2265.0
	$Tight_{(2)}$	2923.4

[a]Respective forms correspond to those observed in various complexes shown in Fig. 1D-F (eA_3B_3, bA_3B_3, and bV_1), Fig. 3C ($eA_3B_{(L65Y)3}$), and Fig. 4D ($bA_3B_{(L65Y)3}$).

Table S4. Sum of contact surface areas at the central domain in A_3B_3 (Å^2).

Structure	Contact surface (Å^2)[a]	
	Intra-A_1B_1 unit	Inter-A_1B_1 unit
eA_3B_3	4837.0	2662.4
bA_3B_3	5561.0	2809.0
$eA_3B_{(L65Y)3}$	4547.3	2772.1
$bA_3B_{(L65Y)3}$	5717.0	2596.1

[a]Sum of all contact surface areas at the central domain between A and B subunits of A_3B_3

Table S5. RMSD values in superimpositions for each A_1B_1 unit of $bA_3B_{(L65Y)3}$ in the crystal structures of A_3B_3 and V_1 complexes.

Structure	Form	$bA_3B_{(L65Y)3}$		
	A_1B_1 unit	$Tight_{(1)}$	Bound	$Tight_{(2)}$
	Empty	4.70	4.17	4.76
eA_3B_3	Bindable	4.79	3.98	4.84
	Bound	2.35	1.53	2.39
	Empty	4.52	3.98	4.55
bA_3B_3	$Bound_{(1)}$	1.75	0.94	1.81
	$Bound_{(2)}$	1.63	0.92	1.69
	Empty	4.54	4.01	4.59
bV_1	Bound	1.69	1.00	1.74
	Tight	0.91	1.63	0.59
	$Bindable_{(1)}$	4.75	3.99	4.80
$eA_3B_{(L65Y)3}$	$Bindable_{(2)}$	4.54	3.76	4.60
	$Bindable_{(3)}$	4.39	3.52	4.44
	$Tight_{(1)}$	0.00	1.54	0.79
$bA_3B_{(L65Y)3}$	Bound	1.54	0.00	1.55
	$Tight_{(2)}$	0.79	1.55	0.00

The values were calculated using Cα atoms.

Descriptions of movies S1 to S4

Movie S1. AFM scan movie of the C-terminal side of the wild-type and mutant A_3B_3. AFM scan movie of the C-terminal side of the wild-type A_3B_3 (upper panel) and mutant $A_3B_{(L65Y)3}$ (lower panel) without nucleotide. Scan area: 30 × 20 nm^2; frame rate: 5 fps.

Movie S2. Conformational changes at the β-barrel domain induced by the mutation. Conformational changes at the β-barrel domain (or crown) of the nucleotide-free A_3B_3 complex induced by the B(L65Y) mutation. The colors and view are consistent with those of fig. S3. Upper panel, side view; lower panel, top view. The video was generated by morphing the X-ray crystal structures of nucleotide-free wild-type (eA_3B_3) and mutant ($eA_3B_{(L65Y)3}$) A_3B_3 using Chimera and PyMOL.

Movie S3. Conformational changes at the C-terminal domain of eA_3B_3 induced by the mutation. Conformational changes at the C-terminal domain of the nucleotide-free A_3B_3 complex induced by the B(L65Y) mutation. The colors and view are consistent with those of Fig. 3C. The video was generated by morphing the X-ray crystal structures of nucleotide-free wild-type (eA_3B_3) and mutant ($eA_3B_{(L65Y)3}$) A_3B_3 using Chimera and PyMOL.

Movie S4. Conformational changes of $eA_3B_{(L65Y)3}$ induced by binding AMP-PNP molecules. Conformational changes of the nucleotide-free mutant $A_3B_{(L65Y)3}$ complex induced by binding three AMP-PNP molecules. The colors and view are consistent with those of Fig. 4A. The video was generated by morphing the X-ray crystal structures of nucleotide-free ($eA_3B_{(L65Y)3}$) and AMP-PNP bound mutant ($bA_3B_{(L65Y)3}$) A_3B_3 using Chimera and PyMOL.